



# Visible-light-driven photocatalytic activity of tiny ZnO nanosheets anchored on NaBiS<sub>2</sub> nanoribbons via hydrothermal synthesis

Ravindranadh Koutavarapu<sup>1</sup> · Gyeongdong Lee<sup>1</sup> · Bathula Babu<sup>1</sup> · Kisoo Yoo<sup>1</sup> · Jaesool Shim<sup>1</sup>

Received: 9 March 2019 / Accepted: 29 April 2019 / Published online: 13 May 2019  
© Springer Science+Business Media, LLC, part of Springer Nature 2019

## Abstract

Novel alkali metal-based NaBiS<sub>2</sub>/ZnO nanocomposite photocatalysts were successfully fabricated via a facile hydrothermal technique for the enhancement of the catalytic activity under visible light. The synthesized photocatalysts were characterized using several microscopic and spectroscopic techniques, which confirmed the formation of heterostructured interfaces between the NaBiS<sub>2</sub> nanoribbons and ZnO nanosheets. The as-prepared NaBiS<sub>2</sub>/ZnO nanocomposites exhibited significantly enhanced photocatalytic performance compared with pure NaBiS<sub>2</sub> and ZnO alone. In particular, a NaBiS<sub>2</sub>/ZnO nanocomposite with ZnO loading of 10 mg achieved rhodamine B (RhB) degradation of 99% under visible-light irradiation within 120 min. The enhanced catalytic performance is ascribed to the synergistic effect of the NaBiS<sub>2</sub> nanoribbons and ZnO nanosheets. The interface between the NaBiS<sub>2</sub> and ZnO allowed the direct transfer of photogenerated electrons, which slowed the recombination of electron–hole pairs and enhanced the charge-separation efficiency. Thus, a probable photocatalytic mechanism is presented for the enhanced degradation of RhB by a NaBiS<sub>2</sub>/ZnO nanocomposite.

## 1 Introduction

Considerable research effort has been directed toward the destruction of organic dye pollutants and attendant environmental remediation using various semiconductor-based photocatalysts under solar-light irradiation. Various semiconductor metal-oxide photocatalysts, such as zinc oxide (ZnO), titanium dioxide (TiO<sub>2</sub>), and tin oxide (SnO<sub>2</sub>), have been applied in these endeavors to improve the photocatalytic performance in the ultraviolet (UV) region [1–5]. Among these, ZnO nanostructures have attracted considerable attention owing to their exceptional optical gain, unique optical and electrical properties, non-toxicity, wide bandgap (~3.37 eV), and good catalytic performance in the UV region [6, 7]. However, the wide bandgap of ZnO limits its applications in the energy-conversion sector, as it can absorb

only 4% of solar radiation in the UV region and is ineffective under visible-light illumination (46%) [8, 9]. To achieve more efficient solar-light energy consumption and improve the photocatalytic activity, novel and efficient visible-light-driven heterostructured photocatalysts have been extensively investigated for the degradation of organic pollutants for environmental conservation.

Alkali-metal-based semiconductors are an interesting class of materials that have recently been shown to have significant scientific potential for application under visible-light irradiation owing to their tunable bandgap and biocompatibility [10, 11]. Among them, sodium bismuth sulfide (NaBiS<sub>2</sub>), an important alkali-metal semiconductor with a bandgap of ~1.22 eV is a particularly promising candidate because of its high chemical stability, non-toxicity, and exceptional photocatalytic activity under visible-light illumination [12]. However, the quick recombination of photoinduced charge carriers in pure NaBiS<sub>2</sub> significantly diminishes its catalytic performance, limiting its practical applications. One effective approach for improving the oxidation ability and photocatalytic activity involves combining a narrow-bandgap semiconductor (NaBiS<sub>2</sub>) with a wide-bandgap semiconductor (ZnO). To the best of our knowledge, no NaBiS<sub>2</sub>/ZnO nanocomposite photocatalysts have been reported thus far.

Ravindranadh Koutavarapu and Gyeongdong Lee have contributed equally to this work.

✉ Kisoo Yoo  
kisooyoo@yu.ac.kr

✉ Jaesool Shim  
jshim@ynu.ac.kr

<sup>1</sup> School of Mechanical Engineering, Yeungnam University, Gyeongsan 712-749, South Korea

Given the foregoing strategies, the construction of alkali metal-based semiconductor heterojunctions is a promising method for enhancing the photocatalytic activity and protecting against hazardous organic contaminants. To this end, Chen et al. successfully constructed heterostructured  $\text{Bi}_2\text{O}_3/\text{Bi}_2\text{S}_3$  photocatalysts using a hydrothermal method. The results indicated that the formation of a heterojunction between  $\text{Bi}_2\text{O}_3$  and  $\text{Bi}_2\text{S}_3$  can improve the separation of photoinduced charge carriers and enhance the photocatalytic activity under visible light [13]. Rong et al. synthesized novel  $\text{Bi}_2\text{S}_3/\text{WO}_3$  composites via a hydrothermal method followed by calcination, and the results suggested that the synergistic interaction of  $\text{Bi}_2\text{S}_3$  and  $\text{WO}_3$  greatly enhanced the photocatalytic degradation of RhB [14]. Gao et al. fabricated a novel  $\text{Bi}_2\text{S}_3/\text{SnS}_2$  nanocomposite using a simple in situ growth method. Experiments revealed that the synergistic effect of  $\text{Bi}_2\text{S}_3$  and  $\text{SnS}_2$  significantly improved the migration of charge carriers, which enhanced the catalytic performance under visible light [15]. The aforementioned results provide sound motivation for the fabrication of  $\text{NaBiS}_2/\text{ZnO}$  nanocomposites with different ZnO loadings using a hydrothermal technique, as such heterostructured nanocomposites may exhibit improved photocatalytic properties.

Herein, we report for the first time the fabrication of novel  $\text{NaBiS}_2/\text{ZnO}$  nanocomposites with a nanoribbon-and-small-nanosheet morphology via a hydrothermal route for enhancing the visible-light-driven photocatalytic performance. The structural and chemical compositions, morphologies, and optical and photocatalytic activity of the as-synthesized materials were characterized precisely. Additionally, according to the results of scavenger experiments and photoluminescence (PL) investigations, a probable photocatalytic mechanism for the enhanced catalytic performance toward the decomposition of RhB dye via visible-light illumination was proposed. The results suggest that the construction of heterostructured  $\text{NaBiS}_2/\text{ZnO}$  nanocomposites is an effective strategy to improve the performance of visible-light-driven photocatalysts for the decomposition of organic pollutants and that these photocatalysts have great potential for application in the fields of sustainable energy and environment.

## 2 Synthesis of photocatalyst

### 2.1 Chemicals

All the chemicals used in this experiment were pure and analytical-grade, and no further purification treatment was performed. Bismuth nitrate ( $\text{Bi}(\text{NO}_3)_3 \cdot 5\text{H}_2\text{O} \geq 98.0\%$ ), sodium sulfide nonahydrate ( $\text{Na}_2\text{S} \cdot 9\text{H}_2\text{O} \geq 98.5\%$ ), zinc acetate ( $\text{Zn}(\text{CH}_3\text{CO}_2)_2 \geq 99.0\%$ ), and sodium hydroxide ( $\text{NaOH} \geq 99.0\%$ ) were purchased from Sigma-Aldrich Co., Ltd., Korea. Polyvinylpyrrolidone (PVP  $\geq 99.0\%$ ),

benzoquinone ( $\text{BQ} \geq 98.0\%$ ), isopropyl alcohol ( $\text{IPA} \geq 99.5\%$ ), triethanolamine ( $\text{TEA} \geq 98.0\%$ ), ethylene glycol ( $\text{C}_2\text{H}_6\text{O}_2 \geq 99.5\%$ ), and ethanol were obtained from Daejung Co., Ltd. Korea. Deionized (DI) water was used for the preparation of all the aqueous solutions.

### 2.2 Synthesis of $\text{NaBiS}_2$ nanoribbons

The  $\text{NaBiS}_2$  nanoribbons used in the experiment were prepared using a hydrothermal technique. In a typical procedure, 0.05 M  $\text{Bi}(\text{NO}_3)_3 \cdot 5\text{H}_2\text{O}$  and an equal molar quantity of  $\text{Na}_2\text{S} \cdot 9\text{H}_2\text{O}$  were dissolved in 100 mL of ethylene glycol, followed by magnetic stirring to obtain a homogeneous solution. The resulting mixture was placed on a hotplate at 100 °C and continuously stirred for 20 min. Thereafter, 2 g of NaOH was added to the mixture, followed by stirring for another 30 min. The suspension was transferred to a 200-mL Teflon-lined autoclave, kept at 120 °C for 12 h, and then cooled to room temperature naturally. Subsequently, the suspension was filtered via centrifugation; washed with DI water, ethanol, and IPA several times; and dried at 80 °C for 8 h.

### 2.3 Synthesis of ZnO nanosheets

ZnO nanosheets were fabricated via a simple low-temperature solution process. Briefly, 0.07 g of PVP was dissolved in 50 mL of ethanol, and the resulting solution was kept on a hotplate at 70 °C and continuously stirred for 10 min. Thereafter, 0.3 g of zinc acetate was added to the mixture, followed by stirring for 10 min. Then, 0.1 g of NaOH was slowly dropped into the solution, with vigorous stirring for 30 min, after which the solution was naturally cooled to room temperature. The obtained white precipitate was centrifuged, rinsed with ethanol and DI water, and dried at 60 °C for 5 h.

### 2.4 Synthesis of $\text{NaBiS}_2/\text{ZnO}$ nanocomposites

$\text{NaBiS}_2/\text{ZnO}$  nanocomposites were successfully fabricated through a facile hydrothermal process. Briefly, 100 mg of  $\text{NaBiS}_2$  nanoribbons was dispersed in 40 mL of absolute ethanol, followed by stirring to obtain a transparent solution (A), and different quantities of ZnO nanosheets (5, 10, and 15 mg) were dissolved in 40 mL of absolute ethanol with stirring to form three variants of another transparent solution (B). Solution B was added dropwise to solution A, with vigorous stirring. After 1 h of stirring, the resulting solution was transferred to a 100 mL Teflon-lined autoclave and maintained at 150 °C for 12 h. Once the autoclave had cooled naturally to room temperature, the precipitates resulting from the three variants of solution B with different amounts of ZnO (hereinafter denoted as NBSZ5, NBSZ10,

and NBSZ15) were collected via centrifugation, rinsed several times with DI water and ethanol, and dried overnight in an oven at 80 °C. The formation mechanism of the NaBiS<sub>2</sub>/ZnO nanocomposite is depicted in Fig. 1.

## 2.5 Characterization of photocatalysts

Powder X-ray diffraction (XRD) studies were performed using a Shimadzu 6100 X-ray diffractometer with Cu K $\alpha$  radiation ( $\lambda = 0.15418$  nm). X-ray photoelectron spectroscopy (XPS) was performed using a Thermo Scientific K-alpha surface analysis instrument. The morphology of the as-prepared samples was analyzed using transmittance electron microscopy (TEM, HITACHI H-7600) and high-resolution TEM (HRTEM, Tecnai G2 F20 S-Twin) at an accelerating voltage of 200 kV. Additionally, the lattice spacings and energy-dispersive X-ray spectroscopy (EDS) color mapping images were investigated. The optical absorption spectra of the as-prepared nanocomposites were analyzed using a Cary 5000 UV–visible–near-infrared (UV–vis–NIR) spectrophotometer. The PL spectra were recorded using a Horiba IHR550 fluorescence spectrophotometer with an excitation wavelength of 325 nm.

## 2.6 Photocatalytic degradation of RhB

The photocatalytic performance of the synthesized nanocomposites was investigated via the decomposition of RhB in an aqueous solution. A 100 W solar simulator was used as a visible-light source for the decomposition of RhB with a  $\lambda > 400$  nm wavelength cutoff filter. The photocatalytic

performance was evaluated using 10 mg of the catalyst and 50 mL of RhB, followed by ultrasonication for 10 min. Before irradiation, the dispersion was kept in the dark for 20 min under magnetic stirring, to attain adsorption–desorption equilibrium of the dye on the surface of the catalyst. Subsequently, the suspension was exposed to visible light for photodegradation. At consistent intervals, 3 mL of the suspension was collected from the photoreactor and centrifuged to separate the photocatalyst. Finally, the concentration of RhB dye was monitored by evaluating the intensity of the absorption peak at 552 nm using a UV–vis–NIR double-beam spectrophotometer. To determine the role of the active radical species during the photocatalytic reaction, the effects of different radical scavengers (IPA as a scavenger for  $\cdot\text{OH}$ , BQ as a scavenger for  $\cdot\text{O}_2^-$ , and TEA as a scavenger for  $\text{h}^+$ ) on the degradation of RhB were investigated. The technique used was similar to that for the aforementioned photocatalytic activity test, except that the radical scavengers (1 mM) were added to the dye solution.

## 3 Results and discussion

### 3.1 XRD study

XRD was used to determine the crystal structure and purity of the as-synthesized nanocomposites, as shown in Fig. 2. The characteristic diffraction peaks (Fig. 2a) located at 26.8°, 31.2°, 45.3°, 53.6°, 55.4°, and 73.1° are attributed to the (111), (200), (220), (311), (222), and (420) planes of the cubic phase of NaBiS<sub>2</sub> (JCPDS #01-075-0065) [16]. For

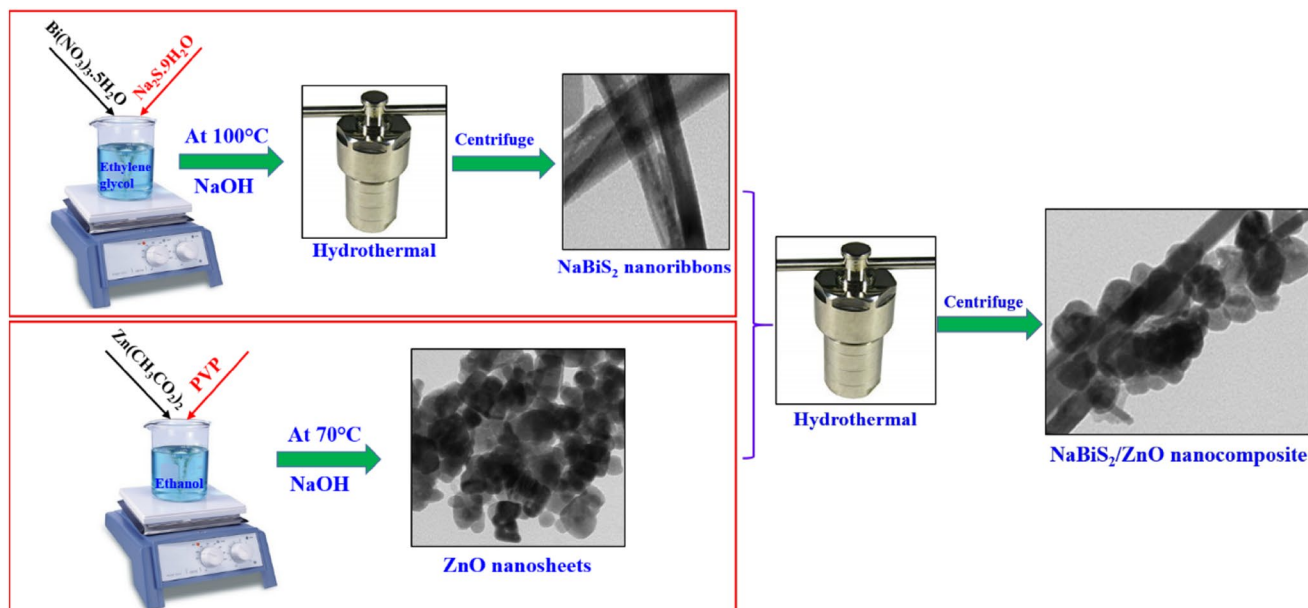
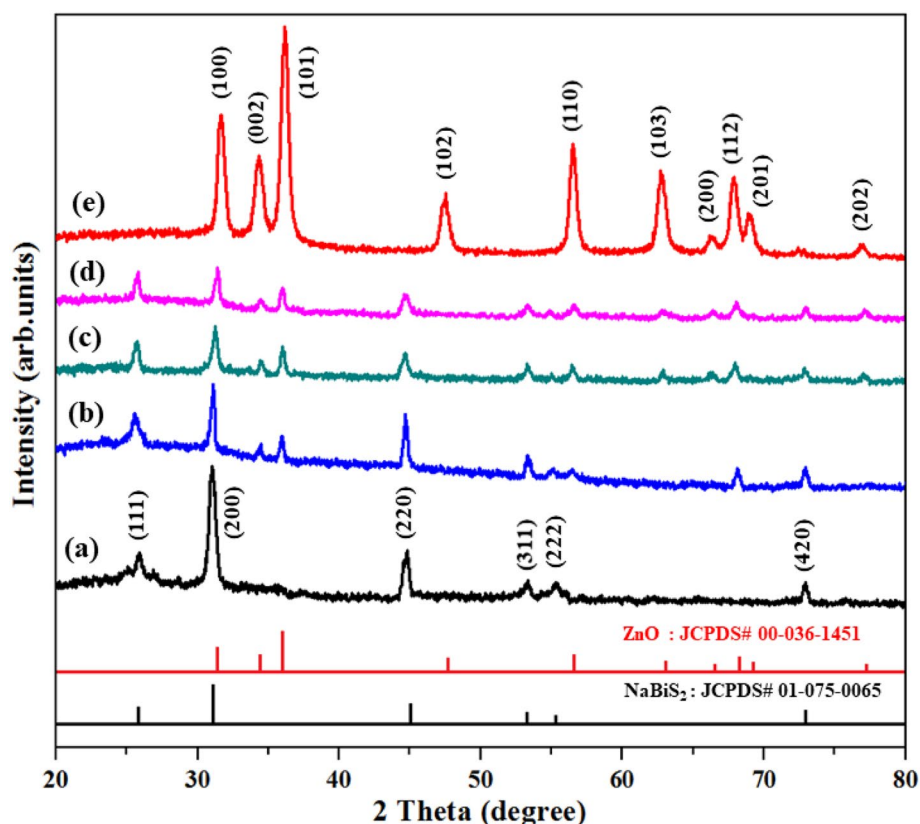


Fig. 1 Schematic of the formation mechanism of the NaBiS<sub>2</sub>/ZnO nanocomposite

**Fig. 2** XRD patterns of (a) pure NaBiS<sub>2</sub>, (b) NBSZ5, (c) NBSZ10, (d) NBSZ15, and (e) pure ZnO



pure ZnO (Fig. 2e), the distinct diffraction peaks detected at 31.6°, 34.3°, 36.17°, 47.5°, 56.5°, 62.8°, 66.2°, 67.9°, 69.0°, and 76.9° correspond to the (100), (002), (101), (102), (110), (103), (200), (112), (201), and (202) planes of the hexagonal wurtzite phase of ZnO (JCPDS #00-036-1451), respectively [17]. Furthermore, all the as-prepared NaBiS<sub>2</sub>/ZnO nanocomposites (Fig. 2b–d) exhibit two sets of characteristic peaks, which are attributed to the cubic NaBiS<sub>2</sub> and hexagonal ZnO, indicating that the NaBiS<sub>2</sub> and ZnO are effectively coupled in the synthesized nanocomposites. With the increase in the ZnO loading, the intensities of the ZnO diffraction peaks increase slightly, while the diffraction-peak intensities of NaBiS<sub>2</sub> decrease. No impurity phases are detected, indicating the high purity of the prepared nanocomposites.

### 3.2 XPS analysis

The surface chemical composition and electronic states of the as-prepared NaBiS<sub>2</sub>/ZnO nanocomposite were investigated via XPS. The survey-scan XPS spectra of the NBSZ10 nanocomposite, which indicated the existence of Na, Bi, S, Zn, and O, is shown in Fig. 3a. The high-resolution XPS spectra of the elements Na, Bi, S, Zn, and O are presented in Fig. 3b–f. The peak centered at 1071.49 eV is attributed to Na 1s (Fig. 3b), which is representative of the Na<sup>+</sup> ions

in NaBiS<sub>2</sub> [18]. In Fig. 3c, the predominant peaks located at 157.89 and 163.17 eV are consistent with Bi 4f<sub>7/2</sub> and Bi 4f<sub>5/2</sub>, respectively, which correspond to the Bi<sup>3+</sup> ions in NaBiS<sub>2</sub>. The weak peaks at 158.91 and 164.28 eV are indexed to the Bi 4f<sub>7/2</sub> and Bi 4f<sub>5/2</sub> signals of the Bi metal, respectively. The peak at 161.66 eV is ascribed to the S 2p signal, whereas the characteristic S 2s peak at 224.86 eV (Fig. 3d) is consistent with the S<sup>2-</sup> in NaBiS<sub>2</sub> [19–21]. As shown in Fig. 3e, the Zn 2p spectra exhibited peaks with binding energies of 1021.57 and 1044.62 eV, which are indexed to Zn 2p<sub>3/2</sub> and Zn 2p<sub>1/2</sub>, respectively [22]. In Fig. 3f, the peaks centered at 530.93, and 532.81 eV are attributed to the binding energies of the O 1s state [23]. The XPS data clearly confirm the formation of the heterostructured NaBiS<sub>2</sub>/ZnO nanocomposite.

### 3.3 Morphological studies

The surface morphologies of pure NaBiS<sub>2</sub>, pure ZnO, and the NaBiS<sub>2</sub>/ZnO nanocomposites were investigated using TEM and HRTEM. Figure 4 shows the TEM images of pure NaBiS<sub>2</sub>, pure ZnO, and the NBSZ5, NBSZ10, and NBSZ15 nanocomposites. As shown in Fig. 4a, the pure NaBiS<sub>2</sub> exhibited nanoribbon-like structures approximately 30–40 nm wide, with a smooth surface. In contrast, the pure ZnO (Fig. 4b) exhibited small nanosheet-like structures

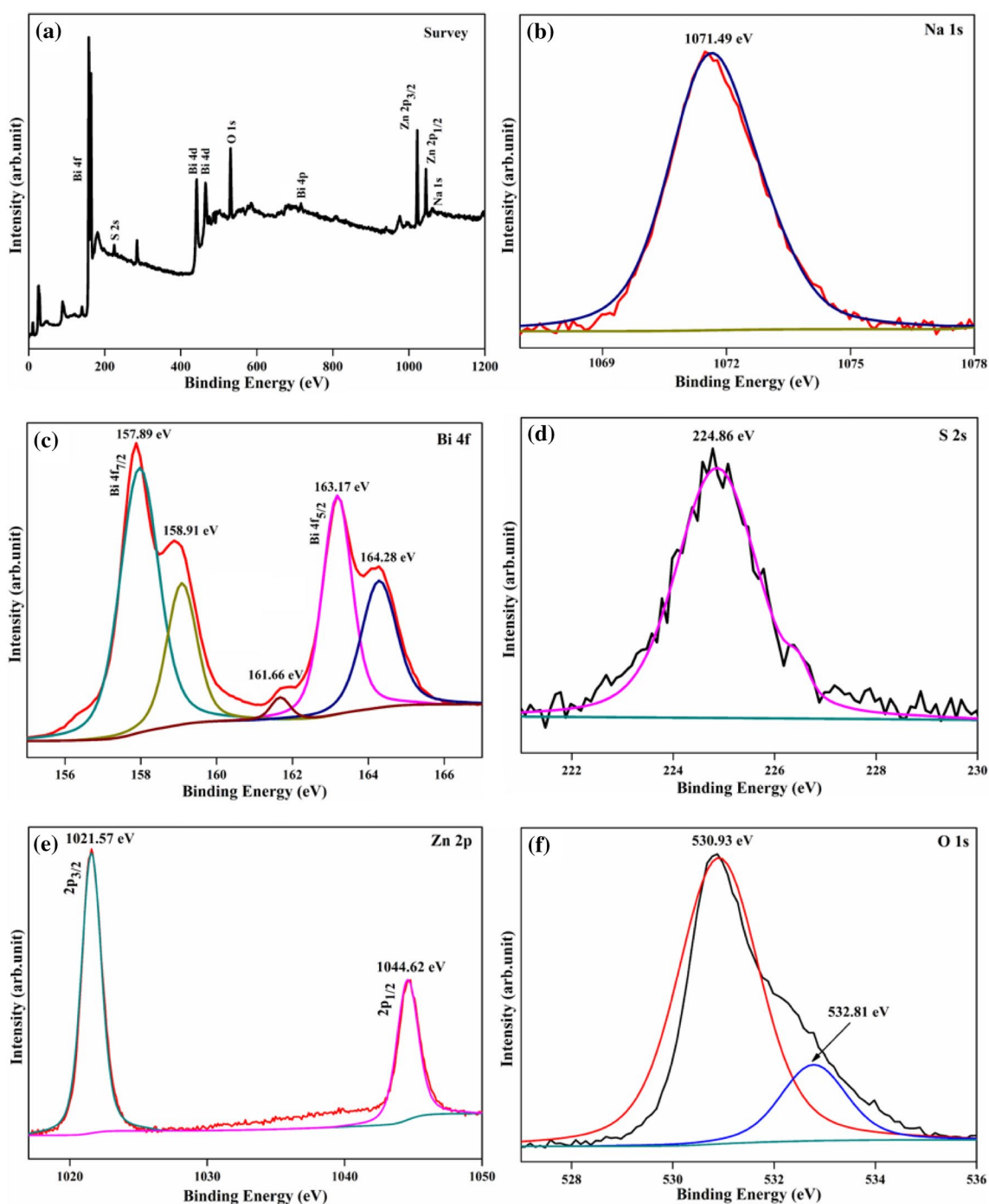


**Fig. 3** High-resolution XPS spectra of the NBSZ10 nanocomposite

approximately 40–50 nm wide. Figure 4c–e show the TEM images of the NBSZ5, NBSZ10, and NBSZ15 nanocomposites, respectively, clearly indicating that the ZnO nanosheets were successfully anchored on the surface of the NaBiS<sub>2</sub> nanoribbons.

HRTEM was used to investigate the lattice fringes of the heterostructured NBSZ10 nanocomposite and perform elemental color mapping. The resultant images are presented

in Figs. 5 and 6. In Fig. 5, two types of lattice spacings are observed in the region; the corresponding *d*-spacings of 0.432 and 0.245 nm are attributed to the (111) plane of NaBiS<sub>2</sub> and the (101) plane of ZnO, respectively [12, 24]. These results clearly indicate the successful formation of a heterostructured interface between NaBiS<sub>2</sub> and ZnO. Additionally, the scanning TEM (STEM)-EDS elemental color mapping patterns of the NBSZ10 nanocomposite presented in Fig. 6a–f confirm the



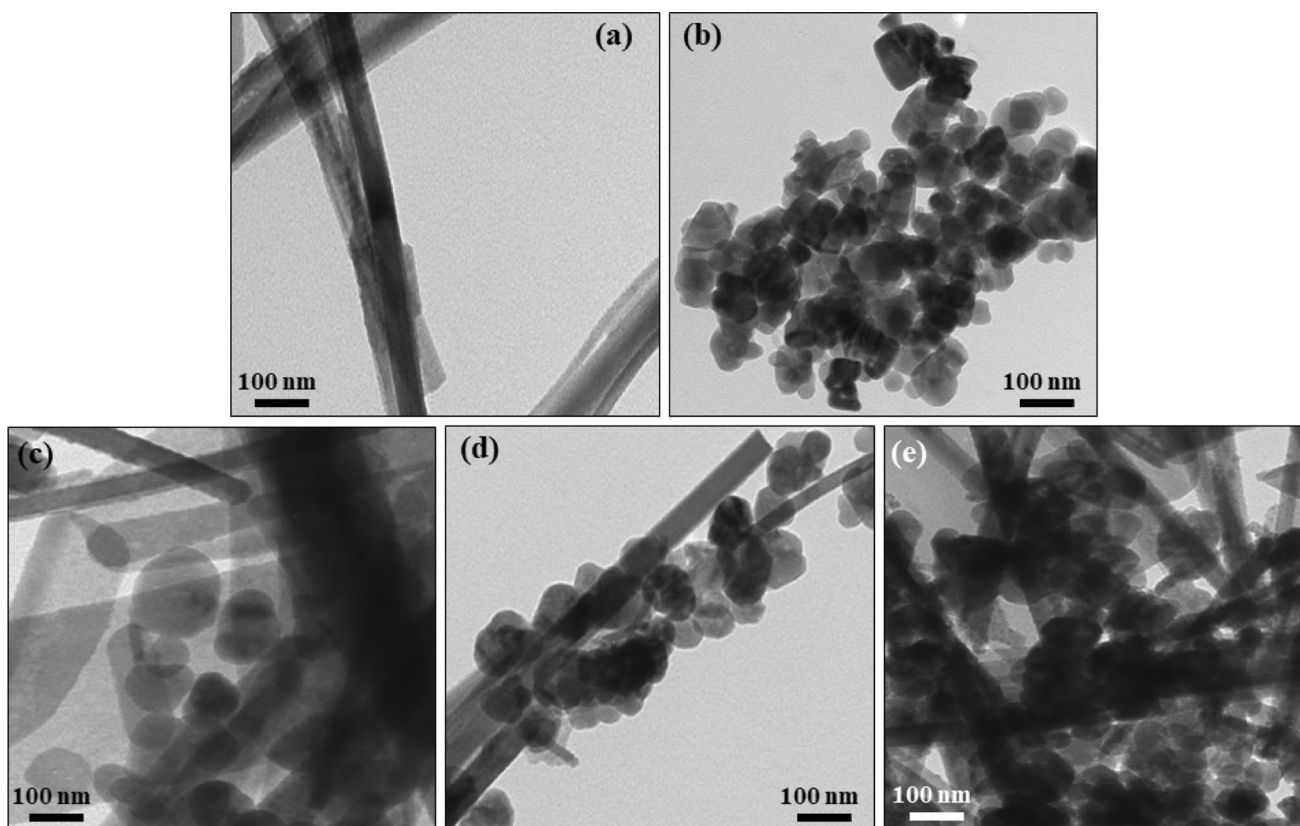


Fig. 4 TEM images of a pure NaBiS<sub>2</sub>, b pure ZnO, and the c NBSZ5, d NBSZ10, and e NBSZ15 nanocomposites

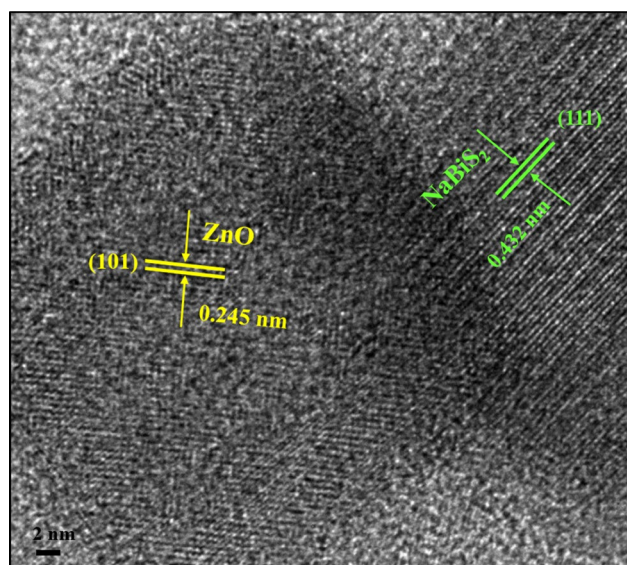


Fig. 5 Lattice fringe pattern of the NaBiS<sub>2</sub>/ZnO nanocomposite (NBSZ10) in the HRTEM image

significant attachment of NaBiS<sub>2</sub> and ZnO. The results agree well with those of the TEM, XRD, and XPS analyses.

### 3.4 Optical absorption and PL studies

UV–Vis absorption spectroscopy was performed to evaluate the light-harvesting proficiency of the as-prepared nanocomposites, and the results are shown in Fig. 7. The absorption band edge of pristine ZnO was around 385 nm, with a bandgap of ~3.22 eV, while that of pure NaBiS<sub>2</sub> was approximately 1032 nm, which is consistent with a bandgap of ~1.20 eV [25, 26]. All the NaBiS<sub>2</sub>/ZnO nanocomposites exhibited a prominent redshift toward the visible-light region, which is attributed to the strong interfacial interaction between NaBiS<sub>2</sub> and ZnO. The significant redshift suggests that most of the visible light was absorbed by the nanocomposite photocatalysts, generating sufficient charge carriers, which greatly enhanced the separation efficiency and photocatalytic activity [27].

The band positions of the synthesized samples were determined using the following empirical formulae:

$$E_{VB} = \chi - E_e + (0.5)E_g$$

$$E_{CB} = E_{VB} - E_g$$

where  $E_{VB}$  and  $E_{CB}$  represent the valence band (VB) and conduction band (CB) potentials, respectively, and  $\chi$  represents the electronegativity of ZnO and NaBiS<sub>2</sub> (5.75 and

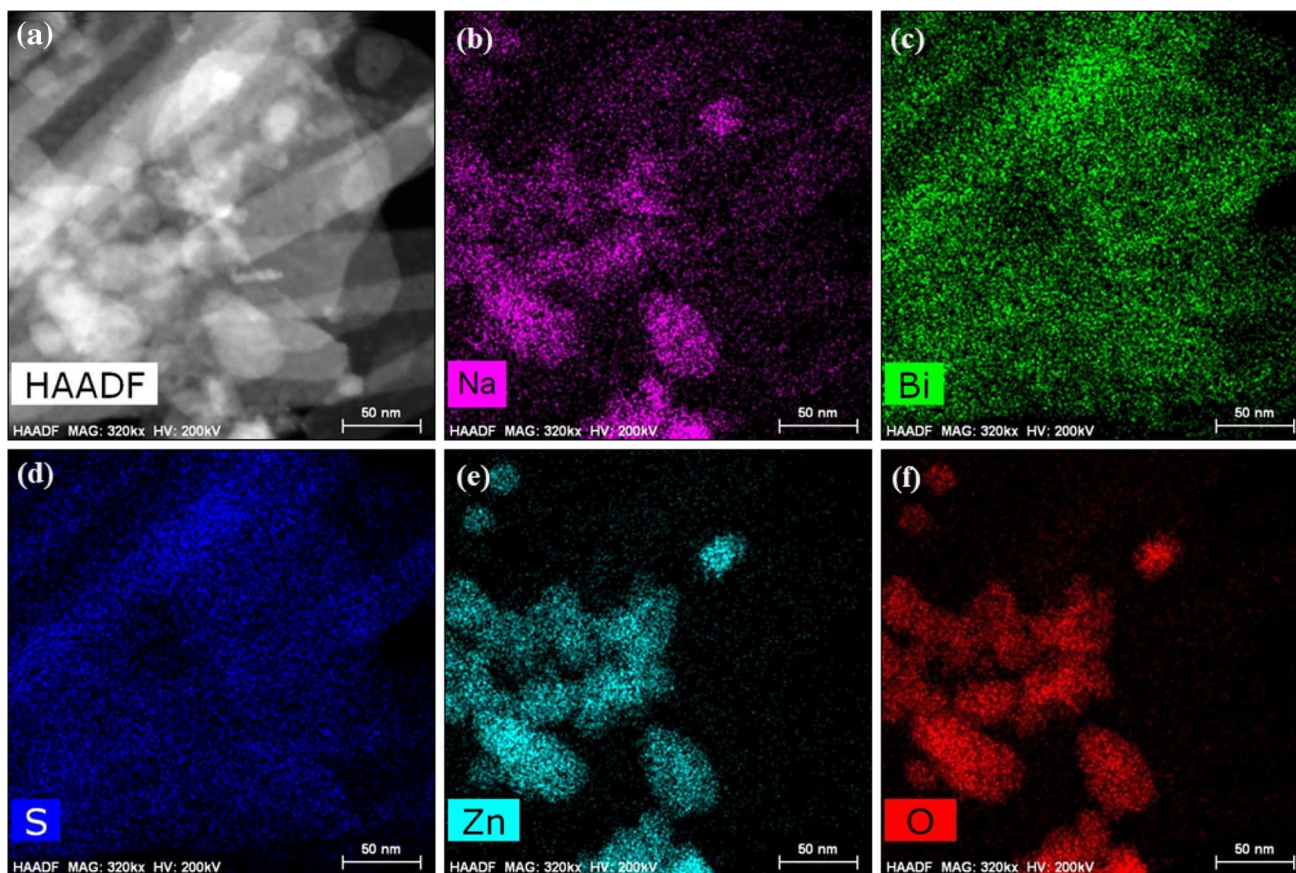
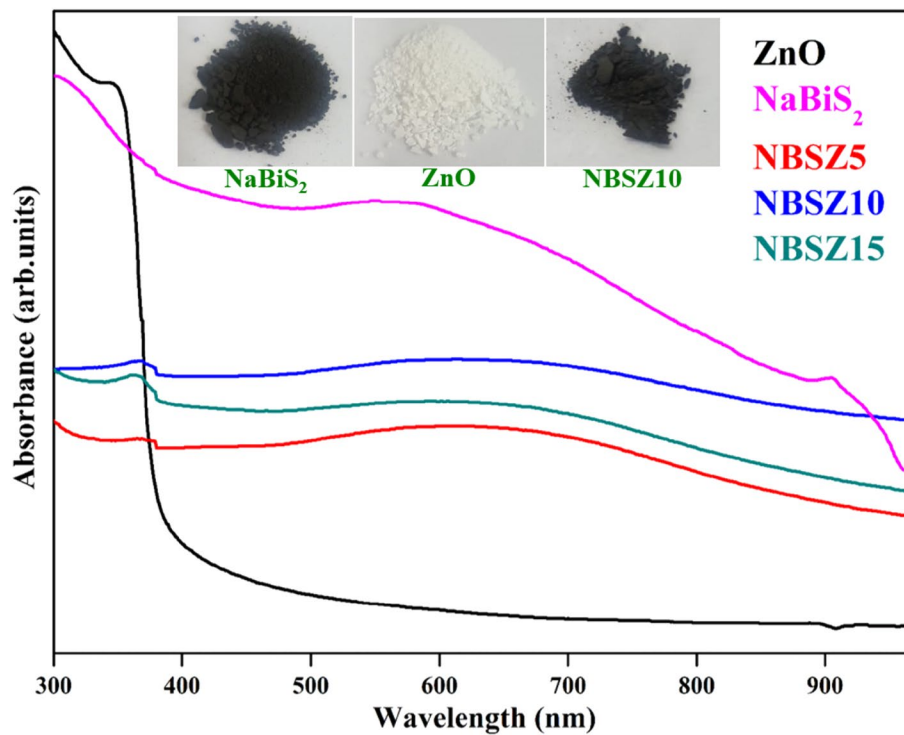


**Fig. 6** STEM-EDS elemental color mapping of the NBSZ10 nanocomposite. **a** Mapping region, **b** Na, **c** Bi, **d** S, **e** Zn, and **f** O

**Fig. 7** Optical absorption spectra of pure  $\text{NaBiS}_2$ , pure  $\text{ZnO}$ , and the NBSZ5, NBSZ10, and NBSZ15 nanocomposites





4.612 eV, respectively).  $E_g$  and  $E_e$  represent the bandgap energy and the energy of free electrons on the hydrogen scale ( $\sim 4.5$  eV), respectively. The  $E_{VB}$  values of ZnO and NaBiS<sub>2</sub> were calculated to be +2.860 and +0.707 eV, respectively, and the  $E_{CB}$  values were measured to be  $-0.360$  and  $-0.493$  eV, respectively.

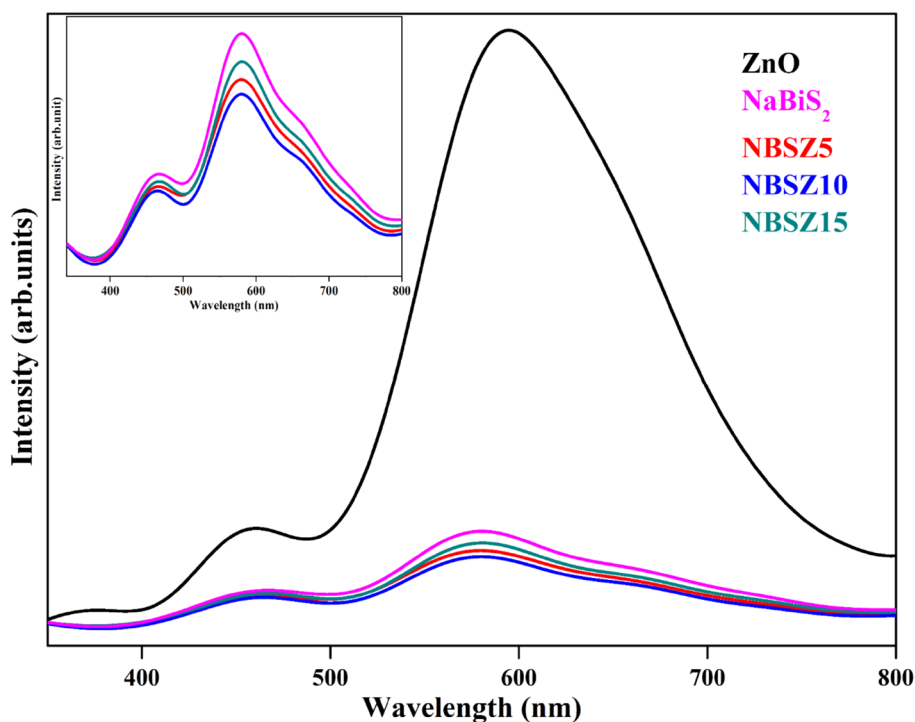
The room-temperature PL spectra of the as-prepared nanocomposites were used to investigate the emission mechanism and the recombination probability of the photogenerated charge carriers, which confirmed the improved catalytic performance of the heterostructured photocatalyst. Figure 8 shows the PL spectra of the as-prepared nanocomposites with an excitation wavelength of 325 nm. The pure ZnO exhibiting a UV emission band around 364 nm is ascribed to the near-band-edge of ZnO, and an emission band is detected at approximately 455 nm, which could be related to constrained excitons and imperfections located on the ZnO surface [28, 29]. The strong PL emission around 593 nm was due to the charge-carrier relaxation caused by the surface-related trap states of O vacancies on the ZnO surface [30]. For NaBiS<sub>2</sub>, the emission band centered at 459 nm is attributed to the intrinsic luminescence of the band edge, and the visible emission band centered at 577 nm was due to point defects such as Bi vacancies and S interstitials in the NaBiS<sub>2</sub> lattice [31, 32]. The electron–hole recombination rate decreased with the addition of ZnO to the composite owing to the formation of the heterojunction between NaBiS<sub>2</sub> and ZnO. However, when the amount of ZnO was significantly increased ( $> 10$  mg), the recombination rate

increased because of the formation of additional junction sites, which acted as recombination sites.

### 3.5 Photocatalytic activity

The visible-light photocatalytic performance of pure NaBiS<sub>2</sub>, pure ZnO, and the NBSZ5, NBSZ10, and NBSZ15 photocatalysts was examined via measurement of the degradation of an RhB solution under solar light irradiation. Figure 9a shows the absorption spectra of RhB under visible light in the presence of the NBSZ10 photocatalyst. The intensity of the characteristic absorption peak of RhB at 552 nm gradually decreased and vanished after 120 min of visible-light irradiation. The changes in the RhB concentration ( $C/C_0$ ) for ZnO, NaBiS<sub>2</sub>, and the NBSZ5, NBSZ10, and NBSZ15 photocatalysts with respect to time are presented in Fig. 9b. In the absence of photocatalysts (darkness), the photodegradation of RhB was unaffected, but the RhB was degraded by 18% and 47% with pure ZnO and NaBiS<sub>2</sub>, respectively. The heterostructured NaBiS<sub>2</sub>/ZnO photocatalysts (NBSZ5, NBSZ10, and NBSZ15) greatly improved the photocatalytic performance compared with pure ZnO and NaBiS<sub>2</sub>: the visible-light-driven RhB degradation for the NBSZ5, NBSZ10, and NBSZ15 photocatalysts was 66, 99, and 53% respectively, within 120 min. Among the photocatalysts, NBSZ10 exhibited the highest degradation efficiency for the decomposition of RhB. At a high ZnO content (15 mg), small ZnO nanosheets agglomerated on the surface of NaBiS<sub>2</sub> nanoribbons and slowed the electron transfer across the NaBiS<sub>2</sub>/

**Fig. 8** PL spectra of pure NaBiS<sub>2</sub>, pure ZnO, and the NBSZ5, NBSZ10, and NBSZ15 nanocomposites





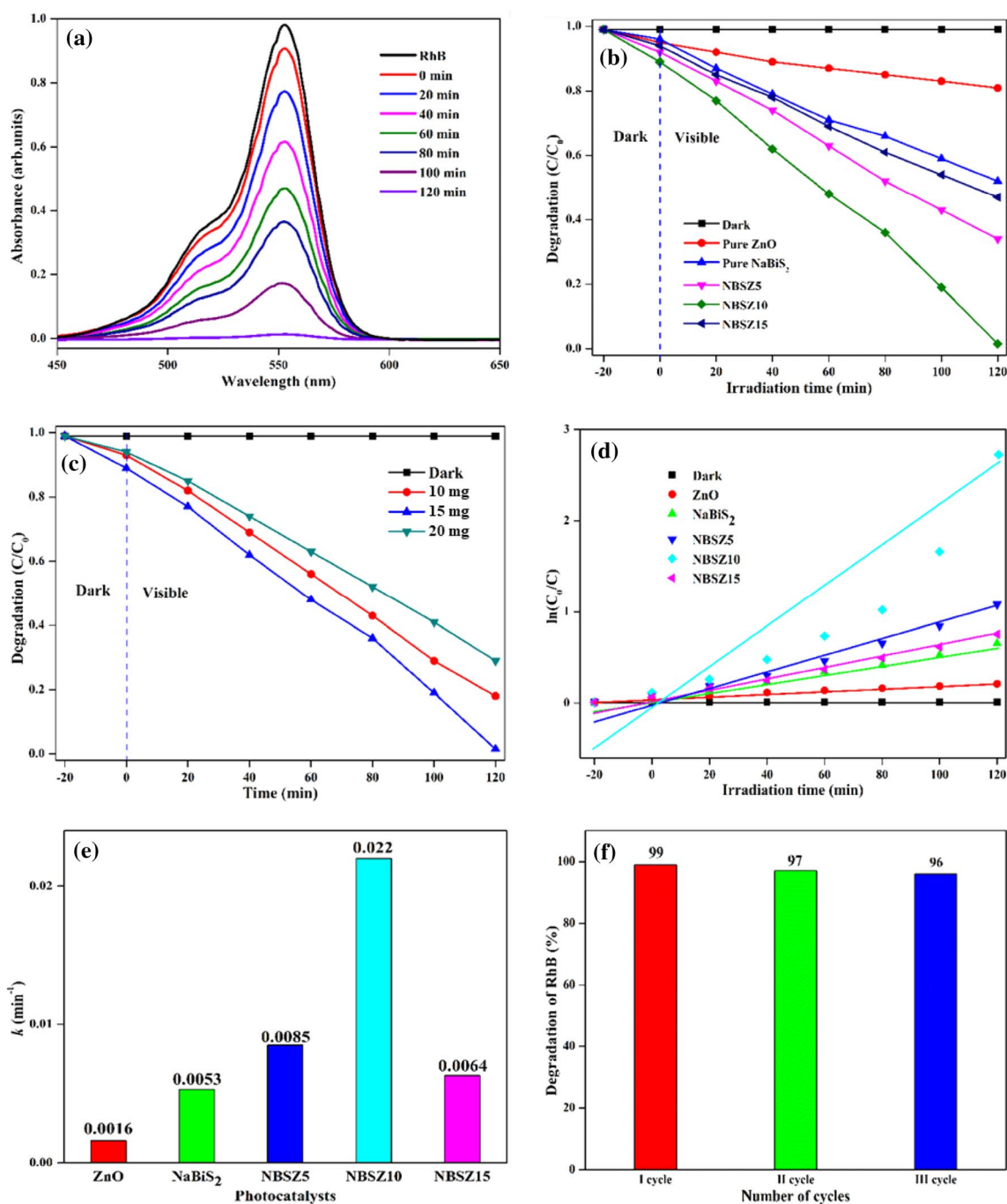


**Fig. 9** **a** Absorption spectra of the NBSZ10 nanocomposite for the photocatalytic degradation of RhB; **b** photodegradation analysis of all the samples; **c** effect of catalyst loading; **d** kinetics of RhB photo-

catalytic degradation:  $[\ln(C_0/C)]$  versus the irradiation time for each catalyst; **e** plot of the  $k$  values; **f** recycling test of the NBSZ10 photocatalyst

ZnO heterojunction interface, reducing the photocatalytic activity [33].

Figure 9c shows the degradation profile of RhB with different loading amounts (10, 15, and 20 mg) of the NBSZ10 catalyst. The NBSZ10 catalyst exhibited better photocatalytic performance at 10 mg than at the other loadings. As the amount of catalyst increased, the photodegradation rate

gradually decreased, possibly because of the agglomeration of particles and the reduction in active sites on the catalyst surface [34]. Thus, overloading a catalyst may negatively affect the rate of RhB degradation. A pseudo-first-order kinetics model was used to assess the catalytic performance of the samples. Figure 9d shows the apparent reaction rate constant ( $k$ ) of RhB dye degradation for each of the prepared

samples. The measured values of  $k$  were 0.0016, 0.0053, 0.0085, 0.022, and 0.0064  $\text{min}^{-1}$  for pure ZnO, pure NaBiS<sub>2</sub>, and the NBSZ5, NBSZ10, and NBSZ15 photocatalysts, respectively (Fig. 9e). Notably, the NBSZ10 catalyst exhibited a significantly higher  $k$  value than the others, and its rate constant for RhB degradation was  $\sim 13.7$  and  $\sim 4.2$  times higher than those of pure ZnO and NaBiS<sub>2</sub>, respectively. The stability of this photocatalyst was examined using cyclic experiments. An NBSZ10 nanocomposite was employed as a characteristic photocatalyst for the removal of RhB dye for three successive test cycles, and the results are shown in Fig. 9f. The NBSZ10 photocatalyst retained its high catalytic performance under similar experimental conditions. These results indicate that the NBSZ10 photocatalyst is highly stable, which supports its practical applicability.

To further investigate the photocatalytic mechanism of the NaBiS<sub>2</sub>/ZnO nanocomposites, trapping experiments were performed with numerous scavengers over the NBSZ10 catalyst to identify the contributions of the main active species to the photodegradation process, as shown in Fig. 10. In this study, the main active species for the degradation of RhB were verified using BQ, TEA, and IPA as the radical scavengers of  $\cdot\text{O}_2^-$ ,  $\text{h}^+$ , and  $\cdot\text{OH}$ , respectively [35]. The photocatalytic performance of the NBSZ10 nanocomposite was significantly inhibited with reductions from 99 to 42% and 57% after the addition of BQ and TEA, respectively (Fig. 10b). The degradation efficiency decreased slightly to 89% with the introduction of IPA, indicating that  $\cdot\text{OH}$  was not the main active species. These results suggest that both the  $\cdot\text{O}_2^-$  and  $\text{h}^+$  radical species played significant roles in the photodegradation process.

According to the foregoing experimental results, a possible mechanism for the improved catalytic activity of the NaBiS<sub>2</sub>/ZnO nanocomposite was proposed, as schematically shown in Fig. 11. Under visible-light treatment, NaBiS<sub>2</sub> can be excited, producing electron–hole pairs. The photogenerated electrons in the CB of NaBiS<sub>2</sub> can quickly migrate to

the CB of ZnO at the close interfacial attachment, as the CB potential of NaBiS<sub>2</sub> ( $-0.493$  eV) is more negative than that of ZnO ( $-0.36$  eV). However, the photoinduced holes in the VB of NaBiS<sub>2</sub> cannot transfer to the VB of ZnO, because the VB potential of NaBiS<sub>2</sub> ( $+0.707$  eV) is less positive than that of ZnO ( $+2.86$  eV). Because the CB potential of ZnO is more negative than  $E^\theta(\text{O}_2/\text{O}_2^-) = -0.046$  eV, the electrons accumulated in the CB of ZnO can be trapped by adsorbed O<sub>2</sub> molecules, resulting in the formation of the reactive radical species  $\cdot\text{O}_2^-$ . Then, the generated  $\cdot\text{O}_2^-$  radicals can directly oxidize organic pollutants. The VB potential of NaBiS<sub>2</sub> is less positive than  $E^\theta(\cdot\text{OH}/\text{H}_2\text{O}) = 2.27$  eV, indicating that the photogenerated holes of NaBiS<sub>2</sub> cannot oxidize H<sub>2</sub>O to form  $\cdot\text{OH}$  radicals. Thus, the photogenerated holes of NaBiS<sub>2</sub> remain in the VB and can directly degrade the organic pollutant. According to the results, the photoinduced reactive species  $\cdot\text{O}_2^-$  and  $\text{h}^+$  were favorable for the photodegradation of RhB dye. This indicates that the photo-assisted electron-transfer technique diminished the recombination of photoinduced charge carriers and significantly improved the photocatalytic performance of the prepared nanocomposites under visible-light illumination.

## 4 Conclusion

A series of heterostructured NaBiS<sub>2</sub>/ZnO nanocomposites were fabricated via a hydrothermal route for the removal of organic pollutants under visible light. XRD results confirmed the cubic phase of NaBiS<sub>2</sub> and the hexagonal wurtzite phase of ZnO. TEM and HRTEM revealed that the ZnO nanosheets were successfully anchored on the surface of NaBiS<sub>2</sub> nanoribbons. Optical and PL studies indicated extended visible-light absorption with a strong interface between NaBiS<sub>2</sub> and ZnO, where the photogenerated charge carriers were efficiently detached and enhanced the photocatalytic activity. The as-prepared nanocomposites

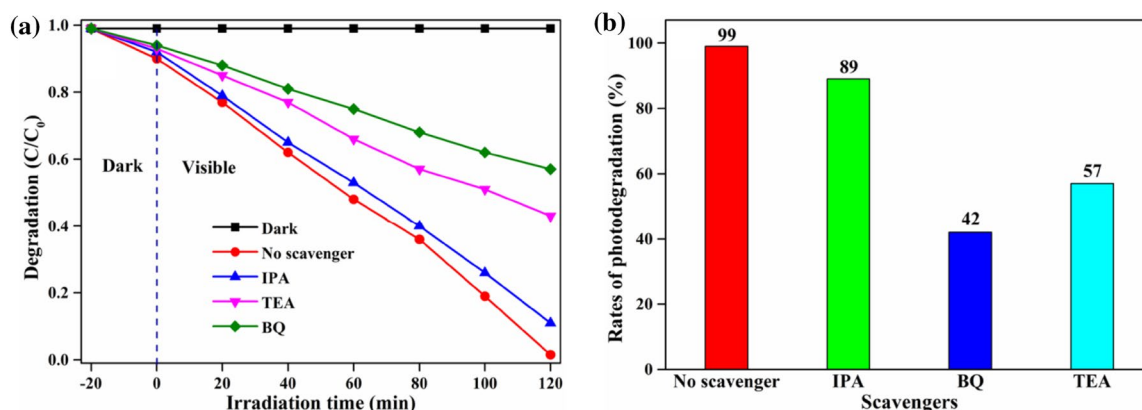
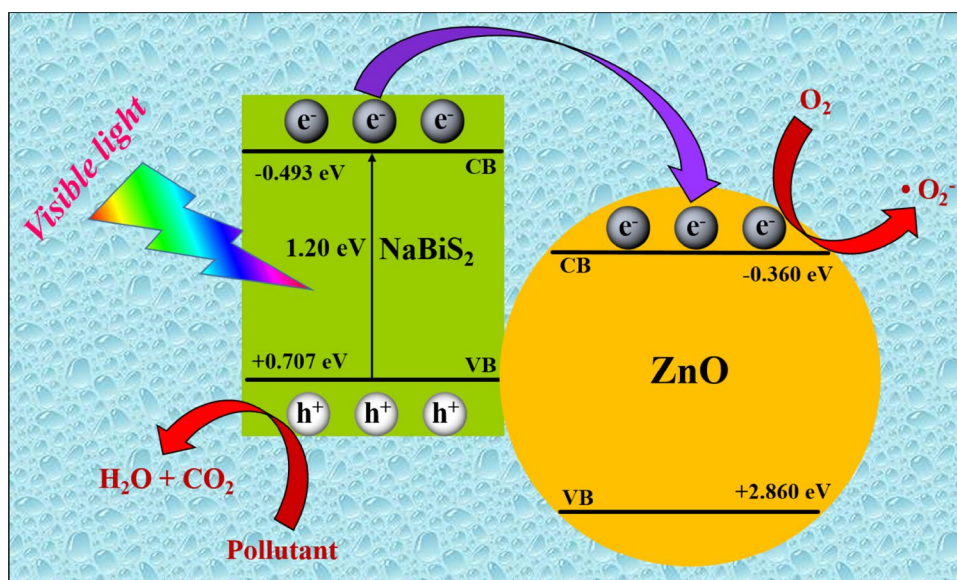


Fig. 10 Control experiment for the degradation of RhB over the NBSZ10 nanocomposite in the absence and presence of scavengers

**Fig. 11** Proposed mechanism for the charge transfer and photocatalytic degradation of RhB in the NaBiS<sub>2</sub>/ZnO nanocomposite



exhibited better catalytic performance than pure NaBiS<sub>2</sub> and pure ZnO. Moreover, the NBSZ10 photocatalyst exhibited exceptional visible-light-driven photocatalytic performance, with ~13.7 and ~4.2 times higher activity for the degradation of RhB dye than pure ZnO and NaBiS<sub>2</sub>, respectively. Thus, the heterojunction of NaBiS<sub>2</sub> and ZnO greatly improved the charge separation and transfer of the photogenerated carriers, significantly enhancing the catalytic performance.

**Acknowledgements** This work was supported in part by a 2019 Yeungnam University Research Grant.

### Compliance with ethical standards

**Conflict of interest** The authors declare that they have no conflict of interest.

### References

- S. Son, P.-H. Jung, J. Park, D. Chae, D. Huh, M. Byun, S. Ju, H. Lee, *Nanoscale* **10**, 21696 (2018)
- D. Smazna, S. Shree, O. Polonskyi, S. Lamaka, M. Baum, M. Zheludkevich, F. Faupel, R. Adelung, Y.K. Mishra, *J. Environ. Chem. Eng.* **7**(103016), 103016 (2019)
- K.R. Reddy, K.V. Karthik, S.B.B. Prasad, S.K. Soni, H.M. Jeong, A.V. Raghu, *Polyhedron* **120**, 69 (2016)
- Y. Xiang, X. Wang, X. Zhang, H. Hou, K. Dai, Q. Huang, H. Chen, *J. Mater. Chem. A* **6**, 153 (2018)
- B. Babu, R. Koutavarapu, V.V.N. Harish, J. Shim, K. Yoo, *Ceram. Int.* **45**, 5743 (2018)
- Y. Zhang, J. Zhou, X. Chen, Q. Feng, W. Cai, *J. Alloys Compd.* **777**, 109 (2019)
- T.B. Demille, R.A. Hughes, A.S. Preston, R. Adelung, Y.K. Mishra, S. Neretina, *Front. Chem.* **6**, 411 (2018)
- C.B. Ong, L.Y. Ng, A.W. Mohammad, *Renew. Sus. Energ. Rev.* **81**, 536 (2018)
- K.R. Reddy, K. Nakata, T. Ochiai, T. Murakami, D.A. Tryk, A. Fujishima, *J. Nanosci. Nanotechnol.* **11**, 3692 (2011)
- T. Ahmad, U. Farooq, R. Phul, *Ind. Eng. Chem. Res.* **57**, 18 (2018)
- J. Jiang, S. Cao, C. Hu, C. Chen, *Chin. J. Catal.* **38**, 1981 (2017)
- B.A. Rosales, M.A. White, J. Vela, *J. Am. Chem. Soc.* **140**, 3736 (2018)
- L. Chen, J. He, Q. Yuan, Y. Liu, C.-T. Au, S.-F. Yin, *J. Mater. Chem. A* **3**, 1096 (2015)
- J. Rong, T. Zhang, F. Qiu, X. Rong, X. Zhu, X. Zhang, *J. Alloys Compd.* **685**, 812 (2016)
- X. Gao, G. Huang, H. Gao, C. Pan, H. Wang, J. Yan, Y. Liu, H. Qiu, N. Ma, J. Gao, *J. Alloys Compd.* **674**, 98 (2016)
- S. Kang, Y. Hong, Y. Jeon, *Bull. Korean Chem. Soc.* **35**, 1887 (2014)
- J. Wang, Y. Xia, Y. Dong, R. Chen, L. Xiang, S. Komarneni, *Appl. Catal. B* **192**, 8 (2016)
- W. Rongchapo, C. Keawkumay, N. Osakoo, K. Deekamwong, N. Chanlek, S. Prayoonpocharach, *J. Wittayakun, Adsorpt. Sci. Technol.* **36**, 684 (2017)
- X. Liu, H. Cao, J. Yin, *Nano Res.* **4**, 470 (2011)
- H.-P. Jiao, X. Yu, Z.-Q. Liu, P.-Y. Kuang, Y.-M. Zhang, *RSC Adv.* **5**, 16239 (2015)
- L. Chen, J. He, Q. Yuan, Y.-W. Zhang, F. Wang, C.-T. Au, S.-F. Yin, *RSC Adv.* **5**, 33747 (2015)
- Y.-C. Liang, C.-C. Wang, *RSC Adv.* **8**, 5063 (2018)
- K.R. Reddy, K. Nakata, T. Ochiai, T. Murakami, D.A. Tryk, A. Fujishima, *J. Nanosci. Nanotechnol.* **10**, 7951 (2010)
- D. Ju, H. Xu, Z. Qiu, J. Guo, J. Zhang, B. Cao, *Sens. Actuator B Chem.* **200**, 288 (2014)
- K.-A. Wong, S.-M. Lam, J.-C. Sin, *Ceram. Int.* **45**, 1868 (2019)
- J. Guo, Z. Ge, M. Hu, P. Qin, J. Feng, *Phys. Status Solidi RRL* **12**, 1800135 (2018)
- H. Xu, Y. Xu, H. Li, J. Xia, J. Xiong, S. Yin, C. Huang, H. Wan, *Dalton Trans.* **41**, 3387 (2012)
- T. Reimer, I. Paulowicz, R. Röder, S. Kaps, O. Lupan, S. Chemnitz, W. Benecke, C. Ronning, R. Adelung, Y.K. Mishra, *A.C.S. Appl. Mater. Inter.* **6**, 7806 (2014)
- Y.K. Mishra, R. Adelung, *Mater. Today* **21**, 631 (2018)
- H.J. Jung, R. Koutavarapu, S. Lee, J.H. Kim, H.C. Choi, M.Y. Choi, *J. Alloys Comp.* **735**, 2058 (2018)



31. A. Rauf, M.S.A. Sher Shah, G.H. Choi, U.B. Humayoun, D.H. Yoon, J.W. Bae, J. Park, W.-J. Kim, P.J. Yoo, ACS Sustain. Chem. Eng. **3**, 2847 (2015)
32. H. Kim, C. Jin, S. Park, W.I. Lee, I.-J. Chin, C. Lee, Chem. Eng. J. **215–216**, 151 (2013)
33. Y. Liu, H. Tang, H. Lv, P. Zhang, Z. Ding, S. Li, J. Guang, Powder Technol. **283**, 246 (2015)
34. K.R. Reddy, C.H.V. Reddy, M.N. Nadagouda, N.P. Shetti, S. Jaesool, T.M. Aminabhavi, J. Environ. Manage. **238**, 25 (2019)
35. S.J. Park, G.S. Das, F. Schütt, R. Adelung, Y.K. Mishra, K.M. Tripathi, T. Kim, NPG Asia Mater. **11**, 8 (2019)

**Publisher's Note** Springer Nature remains neutral with regard to jurisdictional claims in published maps and institutional affiliations.